Speckle effects on time-of-flight estimation of lidar pulses

JEFFREY R. CHEN,* GUANGNING YANG, MARK A. STEPHEN, AND HUI LI

NASA Goddard Space Flight Center, Greenbelt, Maryland, 20771, USA
** jeffrey.r.chen@nasa.gov*

Abstract: Speckle effects particularly impact the performance of compact lidars. The surface roughness and slope spread a received laser pulse to contain M_t temporal speckle cells, distorting the pulse shape and degrading the centroid-based time-of-flight (ToF) estimation. Laser spectral broadening from repeated phase modulation increases M_t and improves the ToF estimation when the surface is significantly rough, but degrades the ToF estimation moderately when the surface is smoother. The solar background and dark noise contributions can be reduced by weighting the waveforms. Line-fitting and plane-fitting to multiple return waveforms are analyzed for precision retrievals of the range rate, slope and range.

1. Introduction

Future space missions call for more compact and efficient lidar instruments, preferably on smaller spacecrafts for cost savings. Such lidars can measure the time of flight (ToF) of laser pulses and the return laser pulse energy, to map the surface in 3-D and retrieve various unknowns (e.g., the surface reflectivity). High efficiency is sought to achieve greater coverage with better precision for the same power constraint. It is also highly desirable to reduce the laser footprint size on the surface for higher spatial resolution. However, illuminating an optically rough surface with a narrower laser beam leads to larger spatial speckle size on the receiver telescope. Using a smaller receiver telescope on a smaller spacecraft further reduces the number of spatial speckle correlation cells M_{sp} falling on the receiver telescope, and thus further increases the speckle noise [1]. The speckle noise degrades the performance of compact lidars that use narrow laser beams and small receiver apertures (such as compact 3D imaging lidars for autonomous vehicles).

The relative variance of the return laser pulse energy arising from the speckle noise is $\sim 1/(M_{sp}M_t)$ where M_t is the number of temporal speckle correlation cells of the received pulse and can be increased by laser spectral broadening [2, 3]. The return laser pulse energy measurement can thus be improved by increasing M_{sp} [1] and broadening the laser linewidth [2]. The optimal time-of-flight estimation is the maximum likelihood (ML) estimation that requires prior knowledge of the mean received pulse shape. However, the surface profile is often not known and the prior knowledge of the mean received pulse shape is not available. Although suboptimal, the ToF can be estimated from the centroid of the received pulse without requiring knowledge of the pulse shape. Such centroid-based ToF estimation is nearly optimal for Gaussian pulses in the shot-noise limited case [4]. In this paper, we analyze speckle effects on the centroid-based ToF estimation for a waveform lidar that transmits laser pulses to the surface and directly detects the return pulses with a linear photon detector. Such a waveform lidar can detect multiple photons simultaneously with single photon sensitivity by using a nearly noiseless HgCdTe avalanche photodiode (APD) detector [5] to achieve close to shot-noise limited performance.

The impact of spatial speckles on the centroid-based ToF estimation has been thoroughly analyzed [4, 6-8], based on a time-resolved treatment of Gardner for large M_{sp} [6]. However, this treatment discounts the speckle noise reduction from the laser spectral broadening, in disagreement with experimental results [2, 3]. In this paper, we extend Gardner's treatment to include the effects of wavelength diversity for the ToF estimation as well as the pulse energy

estimation (see section 2). We quantify speckle effects on the ToF estimation for spectrally broadened laser pulses. To our best knowledge, this work has not been reported previously. Unlike Gardner's treatment, our results remain valid for small M_{sp} (hence relatively smaller lidar footprints and receiver telescopes). It is often desirable to employ fiber laser amplifiers with relatively small fiber cores to increase the wall-plug efficiency. However, the laser lineshape tends to be broadened due to non-linear effects in such small core fibers. Our results in section 3 confirm that such spectral broadening increases M_t and improves the pulse energy estimation. We further show that such spectral broadening improves the ToF estimation when the surface is significantly rough, but degrades the ToF estimation by a tolerable amount when the surface is smoother.

When the laser linewidth is broadened by repeated phase modulation, M_t is the number of coherent intervals contained within a correlation interval of the received pulse. For phase-noise-induced laser spectral broadening, a similar interpretation of M_t has been derived when the received laser field is averaged over an ensemble of uncorrelated speckle patterns for each laser phase noise realization [9]. In section 4, we show that this latter interpretation is not applicable to practical lidar applications where such hypothetical laser field averaging does not occur. Section 5 quantifies the impact of a surface slope on speckle effects. Effects arising from other practical noise sources, including solar background, receiver circuitry, detector dark current, and receiver response jitter are also summarized.

For lidar navigation, the relative speed of the lidar to the target can be derived from the range rate. For 3-D imaging lidars, the range and surface gradient can be retrieved by plane-fitting to lidar returns from laser footprints within a surface area. In section 6, the speckle effects are included to quantify the precision of range rate estimation from multiple pulses and the precision of the plane-fitting. More considerations for the lidar system are discussed in section 7, and further details are provided in the appendix.

2. Treatment of received signal

In this section, we summarize and extend the treatment of Gardner [6]. The geometry of the lidar and an optically rough surface are illustrated in Fig. 1 (*left*) and direct detection receiver model is shown Fig. 1 (*right*). To account for laser spectral broadening, we include a phase modulation (PM) to the field $u_T(\mathbf{r},t)$ of the laser beam at the transmitting aperture

$$\begin{aligned} u_T(\mathbf{r},t) &= a_T(\mathbf{r})a(t)\exp(j2\pi\nu_0 t), \\ a(t) &= |a(t)|\exp[j\phi_m(t)], \end{aligned} \tag{1}$$

where $\phi_m(t)$ represents the deterministic phase modulation that is synchronized to the amplitude modulation (AM) $|a(t)|$, $\mathbf{r}=(x,y)$ is the transverse coordinate vector, $\nu_0 = c/\lambda_0$ the mean laser frequency, λ_0 the mean laser wavelength, and c the speed of light. Here the pulse intensity waveform is normalized (i.e., $\int_{-\infty}^{\infty}|a(t)|^2\,dt=1$) with a rms width of σ_a. The effects of random phase noise is discussed in section 4. For lidar applications of interest, the random laser phase noise is relatively small and its speckle effects are negligible. The transmitted laser beam is scattered back to the receiver by an optically rough surface at a distance z with a surface profile $l(\boldsymbol{\rho})$ where $\boldsymbol{\rho}=(\rho_x,\rho_y)$ is the transverse coordinate vector on the surface. $l(\boldsymbol{\rho})$ can be expressed as $l(\boldsymbol{\rho})=\xi(\boldsymbol{\rho})+\varepsilon(\boldsymbol{\rho})$ where $\xi(\boldsymbol{\rho})$ represents the macrostructure of the surface profile and $\varepsilon(\boldsymbol{\rho})$ the zero-mean random microstructure with a rms value larger than the laser wavelength λ_0. The laser field is assumed to be polarized and the results can be extended for field with arbitrary degree of polarization [9]. Throughout this paper, $\overline{x}$ represents the ensemble average of x and $\delta x \equiv x-\overline{x}$ denotes the deviation from

the mean $\bar{x}$. The mutual coherence function $J_a(\mathbf{r}_1,t_1;\mathbf{r}_2,t_2) \equiv \overline{u^*(\mathbf{r}_1,z,t_1)u(\mathbf{r}_2,z,t_2)}$ of the received optical field $u(\mathbf{r},z,t)$ at the receiving aperture becomes (ignoring some phase factors)

$$J_a(\mathbf{r}_1,t_1;\mathbf{r}_2,t_2) = \frac{T_a^2\beta_r}{z^2}\int d^2\boldsymbol{\rho}\,|\,a_i(\boldsymbol{\rho},z)\,|^2\; a^*(t_1-\psi)a(t_2-\psi)\exp[\,j\frac{2\pi}{z\lambda_0}\boldsymbol{\rho}\cdot(\mathbf{r}_2-\mathbf{r}_1)], \tag{2}$$

where $a_i(\boldsymbol{\rho},z)$ is the complex amplitude of the laser field impinging on the target surface, T_a the one-way atmospheric transmittance, β_r the averaged surface reflectivity (in sr^{-1}), $\psi = \left(2/c\right)\left(z+2\rho^2-\xi(\boldsymbol{\rho})\right)$ is a time delay that varies with surface location $\boldsymbol{\rho}$. Eq. (2) is arrived by neglecting the spatial correlation interval of the surface height that is typically less than 0.1 mm [1]. It can be shown that Eq. (2) remains valid as long as the broadened linewidth of the transmitted laser pulse is much smaller than cz/A_T and $\nu_0\sqrt{A_T/A_R}$, where A_T and A_R are aperture areas of the transmitter and receiver, respectively.

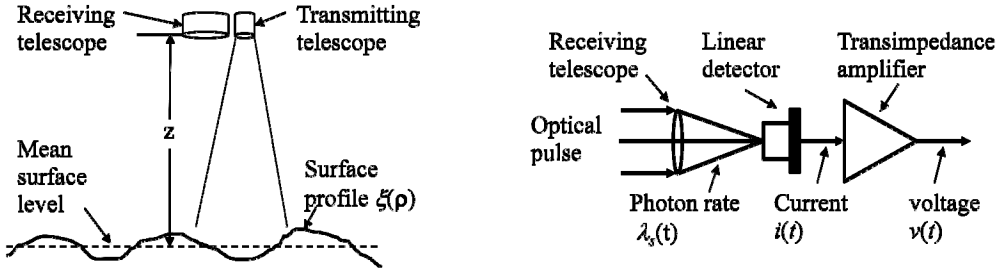

Fig. 1. (*left*) Geometry of the lidar and surface target for normal incidence; (*right*) Block diagram of the direct detection receiver for the pulsed waveform lidar.

As illustrated in Fig. 1 (*right*), the returned photons are collected by a receiving telescope and detected by a linear analog detector, such as an APD, with a mean gain of M_e and a excess noise factor of F_e. The amplified photocurrent $i(t)$ from the detector is further amplified by a transimpedance amplifier (TIA). The voltage output $v(t)$ of the TIA is subsequently digitized and processed to retrieve the ToF, pulse energy and other unknowns. $v(t) = v_s(t) + v_{bgd}$ where $v_s(t)$ arises from the signal photons and v_{bgd} arises from the solar background radiation and the detector dark noise (including the detector dark current and circuitry noise). The signal voltage $v_s(t) = \lambda_s(t) \otimes h(t)$ is a convolution of the received signal photon rate $\lambda_s(t)$ and the receiver impulse response $h(t)$. $h(t) = h_{\text{det}}(t) \otimes h_T(t)$ is a convolution of the detector impulse response $h_{\text{det}}(t)$ and the TIA impulse response $h_T(t)$. The total receiver gain is denoted as $G = \int_{-\infty}^{\infty} h(t)dt$, the impulse delay as $\tau_h = \int_{-\infty}^{\infty} h(t)tdt \Big/ \int_{-\infty}^{\infty} h(t)dt$, and variance of $h(t)$ as $\sigma_h^2 = \int_{-\infty}^{\infty} (t-\tau_h)^2 h(t)dt \Big/ \int_{-\infty}^{\infty} h(t)dt$. Denoting an estimation of $v_s(t)$ as $\hat{v}_s(t) \equiv v(t) - v_{bgd}$, we estimate the ToF of the laser pulse, denoted as T_s , from the centroid of $\hat{v}_s(t)$. t = 0 is set at the centroid of the transmitted pulse $|a(t)|^2$ so that $\int_{-\infty}^{\infty} t\,|a(t)|^2\,dt = 0.$

The mean received photon rate $\overline{\lambda_s(t)}$ is

$$\overline{\lambda_s(t)} = \alpha \int d^2\mathbf{r} J_a(\mathbf{r},t;\mathbf{r},t) w(\mathbf{r}) = \overline{K_s} \int d^2\boldsymbol{\rho} b_2(\boldsymbol{\rho},z) \,|\, a(t-\psi) \,|^2, \tag{3}$$

where $b_2(\boldsymbol{\rho},z) \equiv a_i(\boldsymbol{\rho},z)\,|^2 \,/ \int d^2\boldsymbol{\rho} \,|\, a_i(\boldsymbol{\rho},z)\,|^2$ is the normalized beam intensity incident onto the surface, $w(\mathbf{r})$ the intensity transmittance of the receiver aperture that equal to 1 for $\mathbf{r}$ inside the aperture and zero otherwise, $\alpha \equiv \eta/(h\nu_0)$ is proportional to the detector quantum efficiency η and h is the Planck constant, and $\overline{K_s} = \int_{-\infty}^{\infty} \overline{\lambda_s}(t)dt = \alpha T_a{}^2 \beta_r A_R / z^2 \int d^2\boldsymbol{\rho} \,|\, a_i(\boldsymbol{\rho},z)\,|^2$ is the expected number of detected signal photons per pulse. The covariance $C_{\lambda_s|\xi}(t_1,t_2)$ of $\lambda_s(t)$ (conditioned on a given surface macrostructure $\xi(\boldsymbol{\rho})$) can be expressed as [6]

$$C_{\lambda_s|\xi}(t_1,t_2) = \alpha^2 \int d^2\mathbf{r}_1 \int d^2\mathbf{r}_2 \,|\, J_a(\mathbf{r}_1,t_1;\mathbf{r}_2,t_2)\,|^2 \; w(\mathbf{r}_1) w(\mathbf{r}_2). \tag{4}$$

Eq. (4) is valid when the received field remains to be a circular complex Gaussian process, which is the case despite the repeated AM and PM modulation (see section 4 for details). We now extend Gardner's treatment without making further approximation. From Eq. (2), we arrive at

$$\begin{aligned} C_{\lambda_s|\xi}(t_1,t_2) &= \overline{K_s}^2 \int d^2\boldsymbol{\rho} \int d^2\Delta\boldsymbol{\rho} b_2(\boldsymbol{\rho},z) b_2(\boldsymbol{\rho}+\Delta\boldsymbol{\rho},z) \left|F_w(\Delta\boldsymbol{\rho})\right|^2 \\ &\times a^*(t_1-\psi(\boldsymbol{\rho})) a(t_1-\psi(\boldsymbol{\rho}+\Delta\boldsymbol{\rho})) a(t_2-\psi(\boldsymbol{\rho})) a^*(t_2-\psi(\boldsymbol{\rho}+\Delta\boldsymbol{\rho})), \end{aligned} \tag{5}$$

where $F_w(\Delta\boldsymbol{\rho}) = \int d^2\mathbf{r} w(\mathbf{r}_1) \exp\left(j2\pi\Delta\boldsymbol{\rho}\cdot\mathbf{r}/(z\lambda_0)\right) \Big/ \int d^2\mathbf{r} w(\mathbf{r}_1)$ represents the normalized Fraunhofer diffraction pattern of the receiving aperture [1]. For a uniform circular aperture with a radius of R_R, $\left|F_w(\Delta\boldsymbol{\rho})\right|^2$ is a Airy pattern with most of its power contained within its first zero $\Delta\rho = 0.61 z\lambda_0 / R_R$. The covariance $C_{v_s|\xi}(t_1,t_2)$ of the signal voltage $v_s(t)$ becomes

$$\begin{aligned} C_{v_s|\xi}(t_1,t_2) &= F_e \overline{K_s} \int d^2\boldsymbol{\rho} b_2(\boldsymbol{\rho},z) \int_{-\infty}^{\infty} d\tau \,|\, a(\tau-\psi)\,|^2 \; h(t_1-\tau) h(t_2-\tau) \\ &+ \overline{K_s}^2 \int d^2\boldsymbol{\rho} \int d^2\Delta\boldsymbol{\rho} b_2(\boldsymbol{\rho},z) b_2(\boldsymbol{\rho}+\Delta\boldsymbol{\rho},z) \left|F_w(\Delta\boldsymbol{\rho})\right|^2 \int_{-\infty}^{\infty} d\tau_1 \int_{-\infty}^{\infty} d\tau_2 \\ &\times a^*(t_1-\psi(\boldsymbol{\rho})) a(t_1-\psi(\boldsymbol{\rho}+\Delta\boldsymbol{\rho})) a(t_2-\psi(\boldsymbol{\rho})) a^*(t_2-\psi(\boldsymbol{\rho}+\Delta\boldsymbol{\rho})) h(t_1-\tau_1) h(t_2-\tau_2) \end{aligned} \tag{6}$$

In Gardner's treatment, $\psi(\boldsymbol{\rho}+\Delta\boldsymbol{\rho})$ and $b_2(\boldsymbol{\rho}+\Delta\boldsymbol{\rho},z)$ are in effect approximated by $\psi(\boldsymbol{\rho})$ and $b_2(\boldsymbol{\rho},z)$ for large M_{sp}, thus the surface height fluctuations $(c/2)\left(\psi(\boldsymbol{\rho}+\Delta\boldsymbol{\rho}) - \psi(\boldsymbol{\rho})\right)$ are neglected. However, the Airy patterns for practical lidars are much larger than the 0.1 mm correlation interval of the surface height fluctuations so that $(c/2)\left(\psi(\boldsymbol{\rho}+\Delta\boldsymbol{\rho}) - \psi(\boldsymbol{\rho})\right)$ are not negligible.

3. Estimation of time of flight and pulse energy

The received laser pulse energy is proportional to the integral of the received signal $v_s(t)$

$$\overline{m_0 \,|\, \xi} \equiv \int_{-\infty}^{\infty} \overline{v_s(t)} dt = \overline{K_s} G. \tag{7}$$

The variance of $\overline{m_0 \,|\, \xi}$ arising from the signal $v_s(t)$ can be calculated from Eq. (6):

149
$$\begin{aligned}\mathrm{Var}(m_0|\xi)_{sig} &\equiv \overline{\left[m_0 \mid \xi - \overline{m_0 \mid \xi}\right]^2} = \int_{-\infty}^{\infty} dt_1 \int_{-\infty}^{\infty} dt_2 C_{v_s|\xi}(t_1,t_2) \\ &= F_e \overline{K_s} G^2 + \overline{K_s}^2 G^2 \int d^2\boldsymbol{\rho} \int d^2\Delta\boldsymbol{\rho} b_2(\boldsymbol{\rho},z) b_2(\boldsymbol{\rho}+\Delta\boldsymbol{\rho},z) \left|F_w(\Delta\boldsymbol{\rho})\right|^2 \left|\gamma_a(\tau_{\Delta\xi})\right|^2,\end{aligned} \tag{8}$$

150 where $\gamma_a(\tau_{\Delta\xi}) \equiv \int_{-\infty}^{\infty} d\Delta\tau a^*(\Delta\tau) a(\Delta\tau + \tau_{\Delta\xi})$ is a normalized autocorrelation of the laser pulse
151 modulation $a(t)$, and the time delay $\tau_{\Delta\xi} \equiv \psi(\boldsymbol{\rho}+\Delta\boldsymbol{\rho}) - \psi(\boldsymbol{\rho})$ arises from the surface height
152 difference $\Delta\xi \equiv \xi(\boldsymbol{\rho}+\Delta\boldsymbol{\rho}) - \xi(\boldsymbol{\rho})$. $\tau_{\Delta\xi} \cong 2\Delta\xi / c$ for a narrow laser beam. Assuming a
153 Gaussian laser lineshape $L_a(f) \equiv \left|F_a(f)\right|^2$ where $F_a(f)$ represents the Fourier transform of
154 $a(t)$, $\left|\gamma_a(\tau_{\Delta\xi})\right|^2$ is also Gaussian as given below

155
$$\left|\gamma_a(\tau_{\Delta\xi})\right|^2 = \exp\left(-\tau_{\Delta\xi}^2 \Big/ \left(2\sigma_{\gamma a2}^2\right)\right), \tag{9}$$

156 where $\sigma_{\gamma a2}$ is the standard deviation of $\left|\gamma_a(\tau_{\Delta\xi})\right|^2$. $\sigma_{\gamma a2} = 1/(2\sqrt{2}\pi\sigma_{va})$ where σ_{va} is the
157 standard deviation of the laser lineshape $L_a(f)$. To gain some physical insight, we assume
158 hereafter the surface height profile is a stationary and ergodic random process. Consequently,
159 the average of $\Delta\xi$ over the laser beam footprint can be evaluated by means of an ensemble
160 average. The unconditional $\mathrm{Var}(m_0)_{sig}$ can be obtained by averaging $\mathrm{Var}(m_0|\xi)_{sig}$ over an
161 ensemble of surface profile $\xi(\boldsymbol{\rho})$:

162
$$\mathrm{Var}(m_0)_{sig} = \overline{\mathrm{Var}(m_0|\xi)_{sig}} = \left(\overline{m_0}\right)^2 \left(\frac{F_e}{\overline{K_s}} + \frac{1}{M_{sp} M_{t0}}\right), \tag{10}$$

163 where $M_{t0} \equiv 1 \Big/ \overline{\left|\gamma_a(\tau_{\Delta\xi})\right|^2}$ is the number of temporal speckle cells arising from the surface
164 roughness and laser spectral broadening, $M_{sp} \equiv 1 \Big/ \int d^2\Delta\boldsymbol{\rho} R_{bb}(\Delta\boldsymbol{\rho},z) \left|F_w(\Delta\boldsymbol{\rho})\right|^2$ is the number
165 of spatial speckle cells [1] and $R_{bb}(\Delta\boldsymbol{\rho},z) = \int d^2\boldsymbol{\rho} b_2(\boldsymbol{\rho},z) b_2(\boldsymbol{\rho}+\Delta\boldsymbol{\rho},z)$ is a normalized
166 autocorrelation function of the laser intensity on the surface. The first term of $\mathrm{Var}(m_0)_{sig}$
167 arises from the signal photon shot noise and APD gain noise, and the second term from
168 speckle-induced photon flux fluctuations. As to be shown in section 5, M_{sp} is approximately
169 the ratio of the receiver aperture area to the speckle correlation area when $M_{sp} >> 1$. We
170 further assume the surface height $\xi(\boldsymbol{\rho})$ is a Gaussian process with negligible correlation
171 between $\xi(\boldsymbol{\rho}+\Delta\boldsymbol{\rho})$ and $\xi(\boldsymbol{\rho})$. Consequently, $\Delta\xi$ is also a Gaussian process and
172 $\sigma_{\Delta\xi}^2 = 2\sigma_{\xi}^2$. M_{t0} then becomes

173
$$M_{t0} \equiv \left[\frac{1}{\sqrt{2\pi}\sigma_{\Delta\xi}} \int_{-\infty}^{\infty} d\Delta\xi \left|\gamma_a(\tau_{\Delta\xi})\right|^2 \exp\left(-\frac{(\Delta\xi)^2}{2\sigma_{\Delta\xi}^2}\right)\right]^{-1} = \sqrt{1 + \frac{(2\sigma_{\Delta\xi}/c)^2}{\sigma_{\gamma a2}^2}}. \tag{11}$$

174 M_{t0} in Eq. (11) agrees with Eq. (6.111) in [2] and M_{t0} = 1 when the surface height
175 fluctuations are negligible.

176 The phase delay $4\pi\xi(\boldsymbol{\rho})/\lambda$ of each tiny surface scatterer changes by 2π when the laser
177 frequency is changed by $c/(2\xi(\boldsymbol{\rho}))$. Correspondingly, the speckle pattern decorrelation

occurs when the laser frequency is changed by $c/(2\sigma_\xi)$ [2]. Consequently, broadening the laser lineshape increases M_{t0}. To increase M_{t0} to $\sqrt{2}$ for a rough surface of $\sigma_\xi \cong 5$ mm, for example, the FWHM laser linewdith needs to be broadened to 4 GHz (13 pm for $\lambda_0 = 1\,\mu$m). Further interpretation of M_{t0} is deferred to section 5.

We now turn to the ToF estimation. The mean ToF for a given $\xi(\mathbf{\rho})$ is [6]

$$\overline{T_s \mid \xi} = \overline{\int_{-\infty}^{\infty} t\hat{v}_s(t)dt \Big/ \int_{-\infty}^{\infty} \hat{v}_s(t)dt} = \overline{\tau_h} + \int d^2\mathbf{\rho} b_2(\mathbf{\rho}, z)\psi(\mathbf{\rho}, z) = \overline{\tau_h} + \frac{2z}{c} + \frac{\sigma_i^{\,2}}{cz} - \frac{2}{c}\langle \xi_2 \rangle, \quad (12)$$

where $\sigma_i^{\,2} \equiv \int d^2\mathbf{\rho}\rho^2 b_2(\mathbf{\rho}, z)$ and $\langle \xi_2 \rangle = \int d^2\mathbf{\rho}\xi(\mathbf{\rho})b_2(\mathbf{\rho}, z)$. Here the mean receiver response delay $\overline{\tau_h}$ contributes to $\overline{T_s|\xi}$ and the optical ToF is $\overline{T_s|\xi} - \overline{\tau_h}$. $\sigma_i^{\,2}$ is negligible for a narrow laser beam. The expected value of the mean square pulse width $\sigma_s^{\,2}$ is given by [6]:

$$\begin{aligned} \overline{\sigma_s^{\,2}} &= \sigma_h^{\,2} + \sigma_a^{\,2} + \frac{4}{c^2}\sigma_\xi^{\,2} + (cz)^{-2}\int d^2\mathbf{\rho} b_2(\mathbf{\rho}, z)\left(\rho^2 - \sigma_i^{\,2}\right)^2, \\ \sigma_\xi^{\,2} &\equiv \int d^2\mathbf{\rho} b_2(\mathbf{\rho}, z)\left(\xi(\mathbf{\rho}) - \langle \xi_2 \rangle\right)^2. \end{aligned} \quad (13)$$

The unconditional variance $\mathrm{Var}(T_s)$ of T_s is the sum of three terms: $\overline{\mathrm{Var}(T_s \mid \xi)_{sig}}$ arising from noise in the signal $v_s(t)$, $\mathrm{Var}(T_s)_{bgd}$ from the noise in v_{bgd}, and $\mathrm{Var}(T_s)_{jitter}$ from the jitter of the receiver response delay τ_h. The latter two terms will be incorporated in section 5. $\mathrm{Var}(T_s \mid \xi)_{sig}$ is

$$\begin{aligned} \mathrm{Var}(T_s \mid \xi)_{sig} &\cong \frac{1}{(\bar{K}_s G)^2}\int_{-\infty}^{\infty} dt_1 \int_{-\infty}^{\infty} dt_2 \left(t_1 - \overline{T_s \mid \xi}\right)\left(t_2 - \overline{T_s \mid \xi}\right) C_{v_s|\xi}(t_1, t_2) \\ &= \frac{F_e}{\bar{K}_s}\left(\sigma_a^{\,2} + \int d^2\mathbf{\rho} b_2(\mathbf{\rho}, z)(\delta\psi)^2\right) + \int d^2\mathbf{\rho}\int d^2\Delta\mathbf{\rho} b_2(\mathbf{\rho}, z) b_2(\mathbf{\rho} + \Delta\mathbf{\rho}, z)\left|F_w(\Delta\mathbf{\rho})\right|^2 \\ &\times\left[(\delta\psi)^2\left|\gamma_a(\tau_{\Delta\xi})\right|^2 + \left|R_{taa}(\tau_{\Delta\xi})\right|^2 + \delta\psi\left(R_{taa}(\tau_{\Delta\xi}) + R_{taa}{}^*(\tau_{\Delta\xi})\right)\gamma_a(\tau_{\Delta\xi})\right], \end{aligned} \quad (14)$$

where $R_{taa}(\tau_{\Delta\xi}) \equiv \int_{-\infty}^{\infty} d\Delta t \Delta t a^*(\Delta t) a(\Delta t + \tau_{\Delta\xi})$ is a cross-correlation function between $ta(t)$ and $a(t)$, and $\delta\psi \equiv \psi(\mathbf{\rho}) + \tau_h - \overline{T_s \mid \xi}$. $\delta\psi \cong 2\xi(\mathbf{\rho})/c + (\tau_h - \overline{\tau}_h)$ for a narrow laser beam. The receiver response jitter $(\tau_h - \overline{\tau}_h)$ is neglected for now and will be included in section 5. Evaluating $R_{taa}(\tau_{\Delta\xi})$ also requires knowledge of the phase modulation, in addition to the lineshape $L_a(f)$. We assume the following chirped Gaussian pulse to approximate the laser self phase modulation, to provide physical insight:

$$a(t) = \frac{1}{\sqrt{\sqrt{2\pi}\sigma_a}}\exp\left[-t^2\left(\frac{1}{4\sigma_a^{\,2}} + j\pi k_a\right)\right], \quad (15)$$

where k_a is the rate of the linear frequency chirp. This pulse has a Gaussian lineshape $L_a(f)$ and $1/\sigma_{\gamma a2}{}^2 = 1/(2\sigma_a^{\,2}) + 1/\sigma_{\gamma pm2}{}^2$ where $1/\sigma_{\gamma pm2}{}^2 \equiv 8(\pi k_a \sigma_a)^2$ arises from the phase

202 modulation. With the AM modulation $|a(t)|$ alone, $\sigma_{\gamma a2} = \sqrt{2}\sigma_a$. Averaging $\mathrm{Var}(T_s \mid \xi)_{sig}$
203 over an ensemble of surface macrostructures $\xi(\boldsymbol{\rho})$, we arrived at

$$\mathrm{Var}(T_s)_{sig} = \frac{F_e}{K_s}\left(\sigma_a{}^2 + \int d^2\boldsymbol{\rho} b_2(\boldsymbol{\rho},z)\overline{(\delta\psi)^2}\right) + \int d^2\boldsymbol{\rho}\int d^2\Delta\boldsymbol{\rho} b_2(\boldsymbol{\rho},z) b_2(\boldsymbol{\rho}+\Delta\boldsymbol{\rho},z)$$
204
$$\times\left|F_w(\Delta\boldsymbol{\rho})\right|^2\left[\overline{(\delta\psi)^2}\overline{\left|\gamma_a(\tau_{\Delta\xi})\right|^2} + \overline{\left|R_{taa}(\tau_{\Delta\xi})\right|^2} + \overline{\delta\psi}\overline{\left(R_{taa}(\tau_{\Delta\xi}) + R_{taa}{}^*(\tau_{\Delta\xi})\right)\gamma_a(\tau_{\Delta\xi})}\right]. \quad (16)$$

205 For normal incidence, $\overline{\delta\psi}\overline{\gamma_a(\tau_{\Delta\xi})\left(R_{taa}(\tau_{\Delta\xi}) + R_{taa}{}^*(\tau_{\Delta\xi})\right)}$ can be neglected because both
206 factors $\overline{\delta\psi}$ and $\overline{\gamma_a(\tau_{\Delta\xi})\left(R_{taa}(\tau_{\Delta\xi}) + R_{taa}{}^*(\tau_{\Delta\xi})\right)}$ are approximately zero. Assuming $a(t)$ is
207 nearly symmetric, $\gamma_a(\tau_{\Delta\xi})\left(R_{taa}(\tau_{\Delta\xi}) + R_{taa}{}^*(\tau_{\Delta\xi})\right)$ becomes an odd function of $\tau_{\Delta\xi}$ and thus
208 averaged to zero. $\delta\psi$ depends only on $\boldsymbol{\rho}$ and is uncorrelated to $\tau_{\Delta\xi}$ so that $\delta\psi$ and $(\delta\psi)^2$
209 are averaged separately. For normal incidence, $\mathrm{Var}(T_s)_{sig}$ is found to be

210
$$\mathrm{Var}(T_s)_{sig} = \frac{F_e}{K_s}\left[\sigma_a{}^2 + \left(2\sigma_\xi / c\right)^2\right] + \frac{(2\sigma_\xi / c)^2}{M_{sp}M_{t0}} + \frac{\left(M_{t0}{}^2 - 1\right)\sigma_a{}^2}{2M_{sp}M_{t0}{}^3}. \quad (17)$$

211 Setting M_{t0} = 1, Eqs. (10) and (17) are reduced to Gardener's Formulas [6] where the
212 contribution of $\Delta\xi(\Delta\boldsymbol{\rho})$ to M_{t0} is neglected. Further explanation of Eq. (17) is deferred to
213 section 5.

214 **4. Effects of random laser phase noise**

215 The laser spectral broadening from a random phase noise can be included by multiplying
216 $u_T(\mathbf{r},t)$ in Eq. (1) with $\exp[j\phi_n(t)]$ where the phase noise $\phi_n(t)$ is assumed to be a wide-
217 sense stationary random process. Thus the autocorrelation function
218 $\gamma_n(\tau) \equiv \overline{\exp[j(\phi_n(t_2) - \phi_n(t_1))]}$ depends only on the time difference $\tau = t_2 - t_1$. The mutual
219 coherence function of the received optical field $u(\mathbf{r},z,t)$ can be obtained by replacing
220 $J_a(\mathbf{r}_1,t_1;\mathbf{r}_2,t_2)$ with $\gamma_n(t_2-t_1)J_a(\mathbf{r}_1,t_1;\mathbf{r}_2,t_2)$ in Eq. (2). When the underlying field remains to
221 be a circular complex Gaussian process, Eq. (4) remains valid provided that $|J_a(\mathbf{r}_1,t_1;\mathbf{r}_2,t_2)|^2$
222 is replaced by $|\gamma_n(t_2-t_1)|^2|J_a(\mathbf{r}_1,t_1;\mathbf{r}_2,t_2)|^2$. For analytical convenience, we further assume
223 $\phi_n(t)$ is Gaussian process with $|\gamma_n(\tau)|^2 = \exp[-\tau^2/(2\sigma_{\gamma n2}{}^2)]$. Including such a phase noise, it
224 can be shown that M_{t0} in Eq. (10) becomes

225
$$M_{tn} = \sqrt{1 + \frac{2\sigma_a{}^2}{\sigma_{\gamma n2}{}^2} + \left(\frac{2\sigma_{\Delta\xi}/c}{\sigma_{\gamma 2}}\right)^2}, \quad (18)$$

226 where $1/\sigma_{\gamma 2}{}^2 = 1/(2\sigma_a{}^2) + 1/\sigma_{\gamma pm2}{}^2 + 1/\sigma_{\gamma n2}{}^2$ includes the additional spectral broadening
227 from the phase noise. When $(2\sigma_{\Delta\xi}/c)/\sigma_{\gamma 2}$ is negligible, $M_{tn} = \sqrt{1 + 2\sigma_a{}^2/\sigma_{\gamma n2}{}^2}$ can be
228 interpreted as the number of rms laser coherent intervals $1\Big/\sqrt{1/(2\sigma_a{}^2) + 1/\sigma_{\gamma n2}{}^2}$ contained

within a rms correlation interval $\sqrt{2}\sigma_a$ of $|a(t)|$. Similar M_{tn} has been shown for a top-hat pulse (see, for example, section 6.1.1 of [9]).

In deriving Eq. (18), the underlying received field is assumed to be a circular complex Gaussian process and averaged independently from the phase noise averaging. This requires the field to be scrambled across an ensemble of uncorrelated speckle patterns during each phase noise realization. However, this is not the case for practical lidar applications where the surface profile (hence the speckle pattern) is essentially unchanged during each short pulse (i.e., each realization of $\phi_n(t)$). Thus M_{tn} given by Eq. (18) is not applicable for such lidar applications. This can be further explained as follows. When $(2\sigma_{\Delta\xi}/c)/\sigma_{\gamma 2}$ is negligible, the phase noise and phase modulation do not change the phase delay $4\pi\xi(\boldsymbol{\rho})/\lambda$ of each tiny surface scatterer of a surface realization during each short pulse. The phase noise and phase modulation simply add a phase change $\phi_n(t)+\phi_m(t)$ to the received field without affecting the intensity for a surface realization during each short pulse, and thus do not change the covariance of the laser intensity and hence $C_{\lambda_s|\xi}(t_1,t_2)$ in Eq. (4). As a result, $M_{t0}\cong 1$ rather than $\sqrt{1+2\sigma_a{}^2/\sigma_{\gamma n2}{}^2}$.

The statistics of $u(\mathbf{r},z,t)$ observed by a practical lidar can be analyzed as follows. Let $u(\mathbf{r},z;f)\exp[j2\pi(\nu_0+f)t]$ represents the received field when the illuminating laser frequency is ν_0+f. $u(\mathbf{r},z;f)$ is a circular complex Gaussian process. The total received field $u(\mathbf{r},z,t)=A(\mathbf{r},z,t)\exp(j2\pi\nu_0 t)$ is found by integrating $u(\mathbf{r},z;f)\exp[j2\pi(\nu_0+f)t]$ over frequency, with the Fourier transform $F_{an}(f)$ of $a(t)\exp[j\phi_n(t)]$ as the weighting factor. Thus

$$A(\mathbf{r},z,t)=\int_{-\infty}^{\infty}u(\mathbf{r},z;f)F_{an}(f)\exp(j2\pi ft)df. \tag{19}$$

With repeated AM and PM modulation, $F_{an}(f)$ remains unchanged from pulse to pulse for different surface realizations so that $A(\mathbf{r},z,t)$ remains to be a circular complex Gaussian process. This is because a linear combination of Gaussian variables remains to be Gaussian and the analytical signal representation $A(\mathbf{r},z,t)$ of the zero-mean process is circular [9]. This is not the case when the random phase noise becomes significant so that $F_{an}(f)$ changes randomly from pulse to pulse for different surface realizations. When $F_{an}(f)$ is random, $A(\mathbf{r},z,t)$ becomes noisier than a circular complex Gaussian process and Eq. (18) is no longer valid. For lidar applications of interest, the laser spectral broadening from the phase noise is relatively small (i.e., $1/\sigma_{\gamma n2}{}^2 \ll 1/(2\sigma_a{}^2)+1/\sigma_{\gamma pm2}{}^2$ and $\sigma_{\gamma n2}\gg 2\sigma_{\Delta\xi}/c$) and thus the effects of random laser phase noise will be neglected in the rest of this paper.

5. Impact of surface slope and additional noise sources

The results of previous sections can be adapted to include the effects of the surface slope if the shadowing effects can be neglected. Without losing generality, the surface slope shown in Fig. 2 is along ρ_x direction and the surface height is $\xi'(\boldsymbol{\rho})=\rho_x\tan\phi+\xi(\boldsymbol{\rho}')/\cos\phi$ where $\rho'_x=\rho_x/\cos\phi+\xi(\boldsymbol{\rho}')\tan\phi$ and ϕ is the slope angle. The surface height difference becomes $\Delta\xi'=\Delta\xi/\cos\phi+\Delta\rho_x\tan\phi$. We also assume a Gaussian laser beam profile

$$b_2(\boldsymbol{\rho},z)=\frac{1}{2\pi(z\tan\theta_T)^2}\exp\left[-\frac{\rho^2}{2(z\tan\theta_T)^2}\right], \tag{20}$$

where θ_T is the half divergent angle corresponding to the rms width of the laser intensity. M_{sp} will be reduced if the effective target surface is smaller than the laser beam. Replacing ξ with ξ', the unconditional mean of T_s becomes

$$\overline{T_s} = = \overline{\tau_h} + \frac{2z}{c} + \frac{1}{cz}\sigma_i^2 = \overline{\tau_h} + \frac{2}{c}z(1+\tan^2\theta_T), \tag{21}$$

and the unconditionally expected value of the mean square pulse width σ_s^2 is [6]

$$\overline{\sigma_s^2} = \sigma_h^2 + \sigma_f^2 + (2/c)^2\left(\sigma_\xi/\cos\phi\right)^2 + (2/c)^2 z^2\left(\tan^2\theta_T\tan^2\phi + \tan^4\theta_T\right). \tag{22}$$

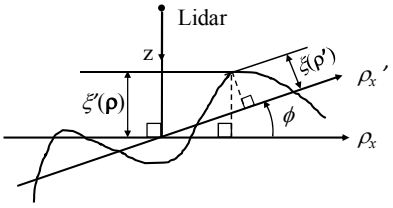

Fig. 2. Geometry of the lidar and surface target for non-normal incidence.

We now evaluate the impact of surface slope on $\mathrm{Var}(m_0)_{sig}$ and $\mathrm{Var}(T_s)_{sig}$. For the Gaussian laser beam, $R_{bb}(\Delta\boldsymbol{\rho}, z)$ is

$$R_{bb}(\boldsymbol{\rho}) = \frac{1}{\pi(2z\tan\theta_T)^2}\exp\left(-\frac{(\Delta\rho)^2}{(2z\tan\theta_T)^2}\right). \tag{23}$$

The Gaussian probability density of surface height difference $\Delta\xi'$ becomes

$$g(\Delta\xi') = \frac{1}{\sqrt{2\pi}\left(\sigma_{\Delta\xi}/\cos\phi\right)}\exp\left(-\frac{\left(\Delta\xi' - \Delta\rho_x\tan\phi\right)^2}{2\left(\sigma_{\Delta\xi}/\cos\phi\right)^2}\right). \tag{24}$$

$\overline{\left|\gamma_a(\tau_{\Delta\xi})\right|^2}$ in $\mathrm{Var}(m_0)$ now depends on $\Delta\rho_x$ due to the slope, as shown below:

$$\overline{\left|\gamma_a(\tau_{\Delta\xi})\right|^2} = \int_{-\infty}^{\infty} d\Delta\xi' \exp\left(-\frac{(2\Delta\xi'/c)^2}{2\sigma_{\gamma a2}^2}\right) g(\Delta\xi') = \frac{1}{M'_{t0}}\exp\left(-\frac{\left(\Delta\rho_x\tan\phi\right)^2}{2(c/2)^2\sigma_{\gamma a2}^2 M'^2_{t0}}\right), \tag{25}$$

where M'_{t0} is the same as M_{t0} given by Eq. (11), except that $\sigma_{\Delta\xi}$ is replaced by $\sigma_{\Delta\xi}/\cos\phi$.

For analytical convenience, the Airy pattern $\left|F_w(\Delta\boldsymbol{\rho})\right|^2$ of a uniform circular aperture can be approximated by a Gaussian function:

$$\left|F_w(\Delta\boldsymbol{\rho})\right|^2 = \left[\frac{2J_1\left(2\pi R_R\Delta\rho/\lambda_0 z\right)}{2\pi R_R\Delta\rho/\lambda_0 z}\right]^2 \cong \exp\left(-\frac{(\Delta\rho)^2}{2\sigma_w^2}\right), \tag{26}$$

where $\sigma_w \equiv \sqrt{2}\lambda_0 z/(2\pi R_R)$ to preserve $\int d^2\Delta\boldsymbol{\rho}\left|F_w(\Delta\boldsymbol{\rho})\right|^2$. This in effect replaces the uniform circular receiver aperture $w(r) = \mathrm{cir}(r/R_R)$ with a circular Gaussian aperture $w(r) = \exp\left(-2r^2/R_R^2\right)$. With this approximation, M_{sp} becomes

$$M_{sp} \equiv 1 \Big/ \int d^2\Delta\boldsymbol{\rho} R_{bb}(\Delta\boldsymbol{\rho}, z) \left| F_w(\Delta\boldsymbol{\rho}) \right|^2 = 1 + \left(\pi R_R \tan\theta_T / \lambda_0 \right)^2 = 1 + A_R / A_{sp}\,, \tag{27}$$

where the speckle correlation area $A_{sp} \equiv \pi {\omega_{0T}}^2$ is the beam waist area of the transmitted Gaussian laser beam with a waist radius of $\omega_{0T} = \lambda_0 / (2\pi \tan\theta_T)$. This confirms that M_{sp} is essentially the number of speckle correlation area falling on the receiver aperture area A_R.

The relative variance of the received pulse energy is found to be

$$\begin{aligned} &\frac{\mathrm{Var}(m_0)_{sig}}{\left(\overline{m_0}\right)^2} = \frac{F_e}{\overline{K_s}} + \frac{1}{M_{sp} M_t}, \\ &M_t \equiv \sqrt{{M'_{t0}}^2 + \left(2\sigma_{\Delta\xi\phi} / c\right)^2 / {\sigma_{\gamma a 2}}^2}\,, \end{aligned} \tag{28}$$

where ${\sigma_{\Delta\xi\phi}}^2 \equiv 2(z \tan\theta_T \tan\phi)^2 / M_{sp}$. $\mathrm{Var}(T_s)_{sig}$ is found from Eq. (16) to be

$$\begin{aligned} \mathrm{Var}(T_s)_{sig} &= \frac{F_e}{\overline{K_s}} \left[{\sigma_a}^2 + \frac{\left(2/c\right)^2 {\sigma_\xi}^2}{\cos^2\phi} + \left(2/c\right)^2 (z \tan\theta_T \tan\phi)^2 \right] + \mathrm{Var}(T_s)_{spec}, \\ \mathrm{Var}(T_s)_{spec} &= \frac{\left(2/c\right)^2}{M_{sp} M_t} \frac{{\sigma_\xi}^2}{\cos^2\phi} + \left(1 + \frac{{M'_{t0}}^2 + 2}{M_{sp} {M_t}^2} \right) \frac{(z \tan\theta_T \tan\phi)^2}{2 M_{sp} M_t} + \frac{\left({M_t}^2 - 1\right) 2 {\sigma_a}^2}{4 M_{sp} {M_t}^3}. \end{aligned} \tag{29}$$

The shot noise contribution $\mathrm{Var}(T_s)_{shot}$ is the first term divided by F_e, and the remaining fraction $(F_e - 1)/F_e$ of the first term arises from the APD gain noise. The second term $\mathrm{Var}(T_s)_{spec}$ arises from the speckle noise. M_t can be interpreted as the number of rms coherent intervals $\sigma_{\gamma a 2}$ contained within a rms correlation interval of the received laser pulse $\sqrt{{\sigma_{\gamma a 2}}^2 + (2/c)^2 \left[\left(\sigma_{\Delta\xi} / \cos\phi \right)^2 + {\sigma_{\Delta\xi\phi}}^2 \right]}$. When a received laser pulse is broadened by the surface height variations to contain M_t temporal speckle cells, the photon flux within each cell is uncorrelated to that of any other cell. This in effect distorts the pulse shape and thereby degrades the ToF estimation. M_t increases with the slope due to additional variance of the surface height difference ${\sigma_{\Delta\xi\phi}}^2$. $\Delta\xi(\Delta\boldsymbol{\rho})$ and the slope contribute to M_t within the Airy pattern. By contrast, $\xi(\boldsymbol{\rho})$ and the slope contribute to the surface height variance within the laser footprint. When $M_{sp} >> 1$, ${\sigma_{\Delta\xi\phi}}^2 / 2$ is much smaller than the additional surface height variance $(z \tan\theta_T \tan\phi)^2$ arising from the slope and $\sigma_{\Delta\xi\phi} \cong \sigma_w \tan\phi$. The factor $\left({M'_{t0}}^2 + 2 \right) \Big/ \left(M_{sp} {M_t}^2 \right)$ in the second term of $\mathrm{Var}(T_s)_{spec}$ is less than $3 / M_{sp}$ and becomes negligible when M_{sp} is large. The last term in $\mathrm{Var}(T_s)_{spec}$ vanishes when $M_t = 1$. Its numerator $\left({M_t}^2 - 1\right) 2 {\sigma_a}^2$ can be expressed as $(2/c)^2 \left({\sigma_{\Delta\xi}}^2 + {\sigma_{\Delta\xi\phi}}^2 \right) \left(\sqrt{2}\sigma_a / \sigma_{\gamma a 2} \right)^2$, increasing quadratically with the normalized laser spectral linewdith $\sqrt{2}\sigma_a / \sigma_{\gamma a 2}$ (normalized by the transform-limited laser pulse spectral linewidth). For the uniform circular aperture $w(r) = \mathrm{cir}(r / R_R)$, the actual $\mathrm{Var}(m_0)_{sig}$ and $\mathrm{Var}(T_s)_{spec}$ are somewhat smaller than derived

above for the Gaussian aperture because the Gaussian approximation of $|F_w(\Delta\boldsymbol{\rho})|^2$ reduces the extend of $\Delta\rho$ by squeezing the outer rings of the Airy pattern into the central lobe.

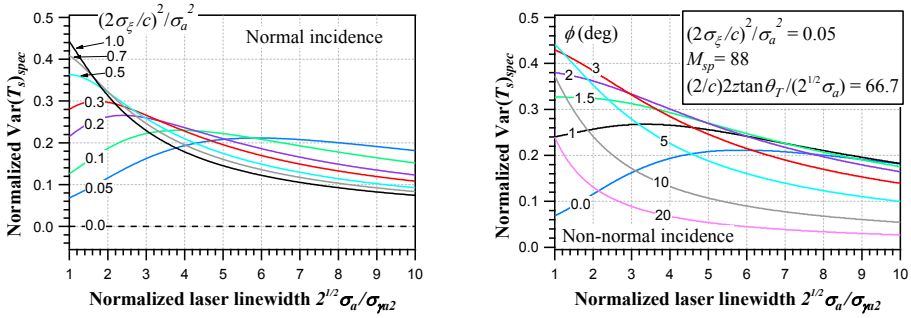

Fig. 3. Var(T_s)$_{spec}$ (normalized by Var(T_s)$_{shot}$ at $\overline{K_s} = M_{sp}$) as functions of the normalized laser pulse linewidth: (*left*) for various values of $(2/c)^2\sigma_\xi^2/\sigma_a^2$ under normal incidence; (*right*) for non-normal incidence at various slope values, and fixed parameters shown in the insert. See text for more details.

The effects of laser spectral broadening on Var(T_s)$_{spec}$ is shown in Fig. 3 where traces of Var(T_s)$_{spec}$ are normalized by the shot noise contribution Var(T_s)$_{shot}$ at $\overline{K_s} = M_{sp}$, and plotted as functions of the normalized linewidth $\sqrt{2}\sigma_a/\sigma_{\gamma a2}$. Figure 3 (*left*) shows plots for various values of the normalized surface roughness $(2/c)^2\sigma_\xi^2/\sigma_a^2$ under normal incidence. Broadening the laser linewidth reduces Var(T_s)$_{spec}$ when $(2/c)\sigma_\xi \geq (\sigma_a/\sqrt{2})$, but increases the normalized Var(T_s)$_{spec}$ to a peak value when the surface is smoother. Figure 3 (*right*) shows plots for non-normal incidence at various slope values, under fixed parameters listed in the insert. These parameters correspond to an Earth-orbiting lidar having a FWHM pulse width of 1 ns, receiving aperture $2R_R$ = 0.5 m, footprint diameter $4z\tan\theta_T$ = 12 m at z = 500 km and σ_ξ = 3.2 mm. When the surface slope angle is increased to a certain level ϕ_t, Var(T_s)$_{spec}$ starts to decrease with increasing laser linewidth. In Fig. 3 (*right*), ϕ_t is only 1.5° so that the laser spectral broadening reduces Var(T_s)$_{spec}$ for most of the terrains. Assuming the same pulse width and σ_ξ for a lunar-orbiting lidar with $2R_R$ = 0.4 m, ϕ_t is increased to 20° when the footprint diameter is reduced to $4z\tan\theta_T$ = 0.85 m at z = 50 km. As shown in Fig 3 (*left*), broadening the laser linewidth improves the worst case ToF measurement and thus beneficial. The maximum increase in Var(T_s)$_{spec}$ with increasing laser linewidth is a small fraction (<16%) of the quantum-limited Var(T_s)$_{shot}$ at $\overline{K_s} = M_{sp}$ and thus tolerable. The first terms in Eqs. (28) and (29) are found by averaging over an ensemble of speckle patterns. The mean of K_s under a dark speckle pattern may become much smaller than its global mean $\overline{K_s}$ so that the contributions from the signal shot noise and APD gain noise may become much larger than the first terms. Increasing the number speckle cells $M_{sp}M_t$ reduces such scintillation effects on the first terms.

The additional noise contributions from v_{bgd} for pulse energy estimation have been summarized in [11]. Each returned pulse is measured in a duration T around its centriod. To reduce the background variance, v_{bgd} can be measured in a longer duration βT between the

pulse measurements, and subtracted from $v(t)$. The additional noise contribution from v_{bgd} to the variance of the ToF is found to be

$$\mathrm{Var}(T_s)_{bgd} = \frac{\lambda_{bgd} T^3}{12\overline{K_s}^2}, \qquad \lambda_{bgd} \equiv (1+1/\beta)\left(F_e \overline{\lambda_{n-n}} + (\alpha P_{NEP})^2/2\right), \tag{30}$$

where λ_{bgd} is a equivalent background noise rate, $\overline{\lambda_{n-n}}$ is the mean detected solar photon rate, P_{NEP} is the single-sided noise-equivalent-power (in $W/\sqrt{Hz}$) of the detector that accounts for the detector circuit noise and dark count rate. The effects the receiver response delay jitter on $\mathrm{Var}(T_s)$ enter through terms proportional to $\overline{\delta\psi^2}$ and is found to be

$$\mathrm{Var}(T_s)_{jitter} = \left(\frac{F_e}{\overline{K_s}} + \frac{1}{M_{sp} M_t}\right)\sigma^2(\tau_h), \tag{31}$$

where $\sigma^2(\tau_h)$ is the variance of receiver response delay τ_h for each detected photon. $\sigma(\tau_h)$ can be as high as 0.3 ns for HgCdTe APD detectors [5] and may impact precision range measurement. In summary, the total ToF variance is given by

$$\mathrm{Var}(T_s) = \mathrm{Var}(T_s)_{sig} + \mathrm{Var}(T_s)_{bgd} + \mathrm{Var}(T_s)_{jitter}. \tag{32}$$

The variance of photon count per pulse is found to be

$$\mathrm{Var}(K_s) = \left(\overline{K_s}\right)^2 \left(\frac{F_e}{\overline{K_s}} + \frac{1}{M_{sp} M_t} + \frac{\overline{\lambda_{bgd}} T}{\overline{K_s}^2}\right). \tag{33}$$

6. Retrievals across multiple laser pulses

When the received photon count per pulse becomes insufficient, it is necessary to aggregate multiple laser pulses to detect their returns and to improve the retrievals of the range and other unknowns. For example, the average range and surface slope can be estimated by linear least squares fitting to returns from consecutive laser footprints along track [12]. The relative speed of the lidar to the target can also be estimated from the range rate using the same concept. The least squares fitting can be extended to plane fitting to estimate the average range and the surface gradient for 3-D imaging [13]. In this section, we quantify the precisions of such estimations under the assumption that return signals of different laser pulses are uncorrelated.

The speckle noise can be averaged down if the speckle noise of each pulse is uncorrelated to that of other pulses. This can be achieved by keeping the laser footprints apart (center to center) by a radius of the receiving aperture (or farther). This can be explained by the same arguments for angle diversity [2]. Consider the worst case where the footprint separation is much smaller than the footprint size so that an adjacent footprint essentially shares the same set of surface scatterers. Then the illumination angle to each scatterer is slightly rotated for the adjacent footprint. The observed speckle pattern is rotated by an amount equal and opposite to the rotation of the illumination angle. For the adjacent footprint, a new set of uncorrelated speckles falls on the receiving aperture. It has also been shown that the observed speckle pattern moves in the opposite direction at the same speed of the lidar that moves in parallel to a stationary surface [10]. Considering an Earth orbiting lidar with an orbiting speed of 7 km/s, the speckle noise becomes uncorrelated when the laser pulses are 71 μs apart for a

receiver telescope as large as 1 m. This is automatically satisfied because the lidar pulses need to be 125 μs apart anyway to avoid cloud folding from clouds 20 km above the surface.

We first estimate the average range and the range rate from returns of n_p laser pulses. Let $\hat{v}_s^{(l)}(t-t^{(l)})$ represent the return waveform of pulse l that is transmitted at a centroid time of $t^{(l)}$ (l = 1, 2, ..., n_p). The ToF of pulse l is denoted as $T_s^{(l)} \equiv \int_{-\infty}^{\infty} dt\hat{v}_s^{(l)}(t)t \Big/ \int_{-\infty}^{\infty} dt\hat{v}_s^{(l)}(t)$. It is convenient to define $\left\langle t^{(l)} \right\rangle \equiv \sum_{l=1}^{n_p} K_s^{(l)} t^{(l)} \Big/ \sum_{l=1}^{n_p} K_s^{(l)}$ as the centroid of $t^{(l)}$ weighted by photon count $K_s^{(l)} = \int_{-\infty}^{\infty} dt\hat{v}_s^{(l)}(t) \Big/ G$, and denote $\Delta t^{(l)} \equiv t^{(l)} - \left\langle t^{(l)} \right\rangle$. As illustrated in Fig. (4) (*left*), all waveforms are aligned by the centroids of the transmitted pulses. By minimizing the following sum of squares of deviations

$$S(T_{sav}, \alpha_t) = \frac{\sum_{l=1}^{n_p} \int_{-\infty}^{\infty} dt\hat{v}_s^{(l)}(t) \left[t - \left(T_{sav} + \alpha_t \overline{\Delta t^{(l)}} \right) \right]^2}{\sum_{l=1}^{n_p} \int_{-\infty}^{\infty} dt\hat{v}_s^{(l)}(t)}, \tag{34}$$

The optimal slope $\hat{\alpha}_t$ and the intercept $\hat{T}_{sav}$ at $\overline{\left\langle t^{(l)} \right\rangle} = \sum_{l=1}^{n_p} \overline{K_s^{(l)}} t^{(l)} \Big/ \sum_{l=1}^{n_p} \overline{K_s^{(l)}}$ are estimated to be

$$\hat{\alpha}_t = \frac{\sum_{l=1}^{n_p} \Delta t^{(l)} \int_{-\infty}^{\infty} dt\hat{v}_s^{(l)}(t)t}{\sum_{l=1}^{n_p} \left(\Delta t^{(l)}\right)^2 \int_{-\infty}^{\infty} dt\hat{v}_s^{(l)}(t)} = \frac{\sum_{l=1}^{n_p} K_s^{(l)} \Delta t^{(l)} T_s^{(l)}}{\sum_{l=1}^{n_p} K_s^{(l)} \left(\Delta t^{(l)}\right)^2}, \tag{35}$$

$$\hat{T}_{sav} = \frac{\sum_{l=1}^{n_p} \int_{-\infty}^{\infty} dt\hat{v}_s^{(l)}(t)t}{\sum_{l=1}^{n_p} \int_{-\infty}^{\infty} dt\hat{v}_s^{(l)}(t)} - \hat{\alpha}_t \delta \left\langle t^{(l)} \right\rangle = \frac{\sum_{l=1}^{n_p} K_s^{(l)} T_s^{(l)}}{\sum_{l=1}^{n_p} K_s^{(l)}} - \hat{\alpha}_t \delta \left\langle t^{(l)} \right\rangle. \tag{36}$$

$\hat{T}_{sav}$ is the averaged ToF starting from $\overline{\left\langle t^{(l)} \right\rangle}$ and the range rate is $(c/2)\hat{\alpha}_t$. From the parallel axis theorem, this is equivalent to line-fitting to data points $(t^{(l)}, T_s^{(l)})$ with error bars defined by Var($T_s^{(l)}$). Reducing the retrieval errors can be visualized as constraining the fitting line from rotating and shifting. The means of $\hat{\alpha}_t$ and $\hat{T}_{sav}$ are estimated from Eq. (34) by replacing $\hat{v}_s^{(l)}(t)$ with the mean waveforms $\overline{\hat{v}_s^{(l)}(t)}$, or equivalently from Eqs. (35) and (36) by replacing $K_s^{(l)}$ with $\overline{K_s^{(l)}}$.

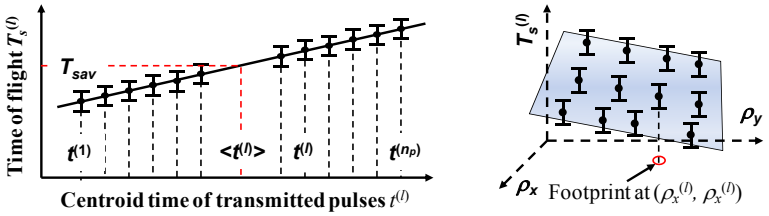

Fig. 4. Illustration of the least squares fitting to return waveforms of multiple pulses: (*left*) line fitting to retrieve the average range T_{sav} and range rate; (*right*) plane fitting to retrieve the average range and surface gradient. Each solid dot represents the centroid of a return

waveform and the corresponding rms error of $T_s^{(l)}$ is depicted by the error bar (see text for more details).

Denoting $\overline{\Delta T_s^{(l)}} \equiv \overline{T_s^{(l)}} - \left(\overline{T_{sav}} + \bar{\alpha}_t \overline{\Delta t^{(l)}}\right)$ as the deviation of $\overline{T_s^{(l)}}$ from the mean fitting line, the variance of the slope $\hat{\alpha}_t$ is found to be

$$\mathrm{Var}(\hat{\alpha}_t) \cong \frac{\sum_{l=1}^{n_p}\left(\overline{K_s^{(l)}}\right)^2\left(\Delta t^{(l)}\right)^2 \mathrm{Var}(T_s^{(l)})}{\left(\sum_{l=1}^{n_p}\overline{K_s^{(l)}}\left(\overline{\Delta t^{(l)}}\right)^2\right)^2} + \frac{\sum_{l=1}^{n_p}\left(\overline{\Delta t^{(l)}}\right)^2\left(\overline{\Delta T_s^{(l)}}\right)^2 \mathrm{Var}(K_s^{(l)})}{\left(\sum_{l=1}^{n_p}\overline{K_s^{(l)}}\left(\overline{\Delta t^{(l)}}\right)^2\right)^2}. \quad (37)$$

The first term arises from the variance of $T_s^{(l)}$ and the second term from the deviations $\overline{\Delta T_s^{(l)}}$. When $\overline{K_s^{(l)}}$, $M_{sp}M_t$ and $\mathrm{Var}(T_s^{(l)})$ are about the same for each pulse, The first term is essentially $\mathrm{Var}(T_s^{(l)}) \Big/ \sum_{l=1}^{n_p}\left(\overline{\Delta t^{(l)}}\right)^2$ and the second term essentially amounts to increase the surface height variance $\sigma_\xi{}^2$ by $\sum_{l=1}^{n_p}\left(\overline{\Delta t^{(l)}}\right)^2\left(\overline{\Delta T_s^{(l)}}\right)^2 \Big/ \sum_{l=1}^{n_p}\left(\overline{\Delta t^{(l)}}\right)^2$. Further neglecting $\overline{\Delta T_s^{(l)}}$, the rms range rate error $\sigma\left(c\hat{\alpha}_t/2\right)$ for a periodically pulsed lidar becomes

$$\sigma\left(c\hat{\alpha}_t/2\right) \cong (c/2)\sqrt{12\,\mathrm{Var}(T_s^{(l)}) \Big/ \left(R_p T_{av}{}^3\right)}, \quad (38)$$

where T_{av} is the averaging time and R_p is the pulse repetition rate. For a practical navigation lidar with a single-pulse rms range error of 3 cm at R_p = 300 kHz, $\sigma\left(c\hat{\alpha}_t/2\right)$ = 0.6 cm/s for T_{av} = 100 ms, satisfying stringent navigation requirements. The variance of $\hat{T}_{sav}$ is found to be

$$\mathrm{Var}(\hat{T}_{sav}) \equiv \overline{\left[\hat{T}_{sav} - \bar{\hat{T}}_{sav}\right]^2} \cong \frac{\sum_{l=1}^{n_p}\left(\overline{K_s^{(l)}}\right)^2 \mathrm{Var}\left(T_s^{(l)}\right)}{\left(\sum_{l=1}^{n_p}\overline{K_s^{(l)}}\right)^2} + \frac{\sum_{l=1}^{n_p}\mathrm{Var}\left(K_s^{(l)}\right)\left(\overline{\Delta T_s^{(l)}}\right)^2}{\left(\sum_{l=1}^{n_p}\overline{K_s^{(l)}}\right)^2}. \quad (39)$$

The first term arises from the variance of $T_s^{(l)}$ and the second term from the deviations $\overline{\Delta T_s^{(l)}}$. When $\overline{K_s^{(l)}}$, $M_{sp}M_t$ and $\mathrm{Var}(T_s^{(l)})$ are about the same for each pulse, the first term is essentially $1/n_p$ of the ToF variance for a single pulse and the second term essentially amounts to increase the surface height variance $\sigma_\xi{}^2$ by $\sum_{l=1}^{n_p}\left(\overline{\Delta T_s^{(l)}}\right)^2 \Big/ n_p$.

We now consider fitting a plane to multiple returns from a 2-D pattern of footprints located at $(\rho_x^{(l)}, \rho_y^{(l)})$ (l = 1, 2, ..., n_p), as illustrated in Fig, 4 (*right*). It is convenient to denote $\Delta\rho_x^{(l)} \equiv \rho_x^{(l)} - \left\langle \rho_x^{(l)} \right\rangle$ and $\Delta\rho_y^{(l)} \equiv \rho_y^{(l)} - \left\langle \rho_y^{(l)} \right\rangle$ where $\left\langle \rho_x^{(l)} \right\rangle = \sum_{l=1}^{n_p} K_s^{(l)}\rho_x^{(l)} \Big/ \sum_{l=1}^{n_p} K_s^{(l)}$ and $\left\langle \rho_y^{(l)} \right\rangle = \sum_{l=1}^{n_p} K_s^{(l)}\rho_y^{(l)} \Big/ \sum_{l=1}^{n_p} K_s^{(l)}$. The optimal fitting parameters minimize the following sum of squares of deviations:

$$S(T_{sav},\alpha_x,\alpha_y)=\frac{\sum_{l=1}^{n_p}\int_{-\infty}^{\infty}dt\hat{v}_s^{(l)}(t)\left[t-\left(T_{sav}+\alpha_x\overline{\Delta\rho_x^{(l)}}+\alpha_y\overline{\Delta\rho_y^{(l)}}\right)\right]^2}{\sum_{l=1}^{n_p}\int_{-\infty}^{\infty}dt\hat{v}_s^{(l)}(t)}. \quad (40)$$

$\hat{T}_{sav}$ is the averaged ToF from the surface point $\left(\overline{\langle\rho_x^{(l)}\rangle},\overline{\langle\rho_y^{(l)}\rangle}\right)$ and $(c/2)(\hat{\alpha}_x,\hat{\alpha}_x)$ is the surface gradient. $(\hat{\alpha}_x,\hat{\alpha}_y)$ is found to be

$$(\hat{\alpha}_x,\hat{\alpha}_y)=\left(\frac{r_{tx}r_{yy}-r_{ty}r_{xy}}{r_{xx}r_{yy}-r_{xy}^2},\frac{r_{ty}r_{xx}-r_{tx}r_{xy}}{r_{xx}r_{yy}-r_{xy}^2}\right), \quad (41)$$

where $r_{tx}\equiv\sum_{l=1}^{n_p}K_s^{(l)}\Delta\rho_x^{(l)}\left(T_s^{(l)}-\overline{T}_{sav}\right)$, $r_{ty}\equiv\sum_{l=1}^{n_p}K_s^{(l)}\Delta\rho_y^{(l)}\left(T_s^{(l)}-\overline{T}_{sav}\right)$, $r_{xx}\equiv\sum_{l=1}^{n_p}K_s^{(l)}\left(\Delta\rho_x^{(l)}\right)^2$, $r_{yy}\equiv\sum_{l=1}^{n_p}K_s^{(l)}\left(\Delta\rho_y^{(l)}\right)^2$, and $r_{xy}\equiv\sum_{l=1}^{n_p}K_s^{(l)}\Delta\rho_x^{(l)}\Delta\rho_y^{(l)}$. $\hat{T}_{sav}$ is obtained by replacing $-\hat{\alpha}_t\delta\langle t^{(l)}\rangle$ in Eq. (36) with $-\hat{\alpha}_x\delta\langle\rho_x^{(l)}\rangle-\hat{\alpha}_y\delta\langle\rho_y^{(l)}\rangle$. The variance $\hat{T}_{sav}$ is also given by Eq. (39) where $\overline{\Delta T_s^{(l)}}$ is the deviation of $\overline{T_s^{(l)}}$ from the mean fitting plane. We further consider a simplified case where the cross correlation r_{xy} is negligible. This is the case when the n_p laser footprints have the same $\overline{K_s^{(l)}}$ and form a rectangular 2-D array on the target surface with equally-spaced rows along ρ_x direction and equally-spaced columns along the ρ_y direction. In this case, $\hat{\alpha}_x$ (or $\hat{\alpha}_y$) becomes identical to $\hat{\alpha}_t$ in Eq. (35) and the variance of $\hat{\alpha}_x$ (or $\hat{\alpha}_y$) becomes identical to $\mathrm{Var}(\hat{\alpha}_t)$ in Eq. (37) provided that $\Delta t^{(l)}$ is replaced by $\Delta\rho_x^{(l)}$ (or $\Delta\rho_y^{(l)}$). The line fitting and plane fitting improve the ToF estimation and also enable precision slope retrievals.

7. Discussion

To increase the lidar efficiency, it is desirable to reduce other noise contributions to achieve close to shot-noise limited performance. The APD detector gain noise contribution is (F_e-1) times of the signal shot noise contribution $\mathrm{Var}(T_s)_{shot}$. For HgCdTe APD detector with $F_e\cong$ 1.2, this is only 20% of the shot noise contribution. A high transimpedance TIA is preferred as the front-end to minimize the impact of circuit noise while allowing sufficient bandwidth. With sufficient APD gain (e.g., > 300), the circuit noise contribution can be reduced to a small fraction of the shot noise contribution.

It is often required for 3-D imaging lidars to map surfaces rapidly and precisely. This can be achieved by transmitting stronger laser pulses and detecting the stronger returns with a sensitive linear detector. This in turn requires higher $M_{sp}M_t$ to keep the speckle noise contribution a small fraction of the shot noise contribution. Stronger laser pulses also overcome the solar background radiation and detector dark noise. The solar background photons can be rejected spectrally with an optical bandpass filter, and spatially by limiting the field of view of the receiver. The laser lineshape can be broadened to increase M_t. M_{sp} can be increased by using a receiver aperture significantly larger than the transmitting aperture. This is not the case for an optical heterodyne lidar where M_{sp} is limited to ≤ 4 for optimal coherent detection efficiency [14].

Although broadening of the electrical signal $v_s(t)$ by the receiver does not increase the noise contributions from the laser signal, the broadening increases the contribution from the noise background v_{bgd}. The ToF variance from v_{bgd} is proportional to T^3, increasing 8 times when T is doubled. The background noise contribution can be reduced by weighting $\hat{v}_s(t)$ iteratively with a window function around the centoid determined from the last iteration. Such windowing techniques have been developed to compute centroids of 2D images [15, 16]. Similarly, each of the waveforms $\hat{v}_s^{(l)}$ for the line fitting or plane fitting can also be weighted iteratively by such a window function centered around the fitting line or fitting plane, to reduce the background noise contribution and reject outliers [13].

8. Conclusions

Speckle effects particularly impact the performance of compact lidars that use narrow laser beams and small receiver apertures. The surface roughness and slope spread the received laser pulse to contain M_t temporal speckle cells, distorting the pulse shape and degrading the ToF estimation. When the linewidth is broadened from repeated phase modulation, M_t is the number of coherent intervals contained within a correlation interval of the received pulse. Such laser spectral broadening increases M_t and thereby improves the laser pulse energy measurement. By contrast, such laser spectral broadening improves the ToF estimation when the surface is significantly rough, but degrades the ToF estimation by a tolerable amount when the surface is smoother. The surface roughness and slope contribute to M_t within the Airy pattern for the receiving aperture, but contribute to surface height variance within the laser footprint. The solar background and detector dark noise contributions can be reduced by weighting the return waveforms with window functions. The range rate can be retrieved precisely by line-fitting to multiple return waveforms. The averaged range, along with the surface gradient, can be retrieved more precisely by plane fitting to multiple return waveforms.

9. Appendix

This appendix summarizes some intermediate steps leading the final results. The cross-correlation function $R_{taa}(\tau_{\Delta\xi})$ in Eq. (16) is found to be

$$R_{taa}(\tau_{\Delta\xi}) \equiv \int_{-\infty}^{\infty} d\Delta t_1 \Delta t_1 a^*(\Delta t_1) a(\Delta t_1 + \tau_{\Delta\xi}) = \left(-1 + j4\pi\sigma_a{}^2 k_a\right) \frac{\tau_{\Delta\xi}}{2} \exp\left(-\frac{\tau_{\Delta\xi}{}^2}{4\sigma_{\gamma a}{}^2}\right). \quad (42)$$

For normal incident, the ensemble average of $\left|R_{taa}(\tau)\right|^2$ becomes

$$\overline{\left|R_{taa}(\tau_{\Delta\xi})\right|^2} = \frac{\sigma_a{}^2}{2} \frac{M_{t0}{}^2 - 1}{M_{t0}{}^3}. \quad (43)$$

This result is used in Eq. (16) to arrive at Eq. (17).

For non-normal incidence, $\overline{\left[\delta\psi(\rho_x)\right]^2}$ and $\overline{\delta\psi(\rho_x)}$ depend on ρ_x, and $\overline{\left|\gamma_a(\tau_{\Delta\xi})\right|^2}$, $\overline{\left|R_{taa}(\tau_{\Delta\xi})\right|^2}$ and $\overline{\left(R_{taa}(\tau_{\Delta\xi}) + R_{taa}{}^*(\tau_{\Delta\xi})\right)\gamma_a(\tau_{\Delta\xi})}$ depend on $\Delta\rho_x$. The following results are used in Eq. (16) to arrive at Eq. (29) . The following two integrals that contain $\overline{\left[\delta\psi(\rho_x)\right]^2}$ are found to be

$$R_{b\delta\psi 2} \equiv \int d^2\boldsymbol{\rho} b_2(\boldsymbol{\rho}, z) \overline{\left[\delta\psi(\rho_x)\right]^2} = (2/c)^2 \left(\sigma_\xi / \cos\phi\right)^2 + (2/c)^2 (z \tan\theta_T \tan\phi)^2, \quad (44)$$

$$R_{bb\delta\psi 2}(\Delta\boldsymbol{\rho}) \equiv \int d^2\boldsymbol{\rho} b_2(\boldsymbol{\rho},z) b_2(\boldsymbol{\rho}+\Delta\boldsymbol{\rho},z) \overline{\left[\delta\psi(\rho_x)\right]^2}$$

503
$$= \left(\frac{2}{c}\right)^2 \exp\left(\frac{-(\Delta\rho)^2}{(2z\tan\theta_T)^2}\right)\left(\frac{\left(\sigma_\xi/\cos\phi\right)^2 + (z\tan\theta_T)^2\tan^2\phi/2}{\pi(2z\tan\theta_T)^2} + \frac{\tan^2\phi\left(\Delta\rho_x\right)^2}{4\pi(2z\tan\theta_T)^2}\right). \quad (45)$$

504 The following integral that contains $\overline{\delta\psi(\rho_x)}$ are found to be

$$R_{bb\delta\psi}(\Delta\boldsymbol{\rho}) \equiv \int d^2\boldsymbol{\rho} b_2(\boldsymbol{\rho},z) b_2(\boldsymbol{\rho}+\Delta\boldsymbol{\rho},z) \overline{\delta\psi(\rho_x)}$$

505
$$= -\frac{2}{c}\frac{\Delta\rho_x\tan\phi}{2\pi(2z\tan\theta_T)^2}\exp\left(-\frac{(\Delta\rho)^2}{(2z\tan\theta_T)^2}\right). \quad (46)$$

506 $\overline{\left|R_{taa}(\tau_{\Delta\xi})\right|^2}$ is found to be

$$\overline{\left|R_{taa}(\tau_{\Delta\xi})\right|^2} = \int_{-\infty}^{\infty} d\Delta\xi' \overline{\left|R_{taa}(2\Delta\xi'/c)\right|^2} g(\Delta\xi')$$

507
$$= {\sigma_a}^2\left[\frac{{M'_{t0}}^2-1}{2{M'_{t0}}^3} + \frac{\left(2\Delta\rho_x\tan\phi/c\right)^2}{2{M'_{t0}}^5{\sigma_{\gamma a2}}^2}\right]\exp\left(-\frac{\left(2\Delta\rho_x\tan\phi/c\right)^2}{2{\sigma_{\gamma a2}}^2{M'_{t0}}^2}\right). \quad (47)$$

508 $\overline{\left(R_{taa}(\tau_{\Delta\xi}) + R_{taa}{}^*(\tau_{\Delta\xi})\right)\gamma_a(\tau_{\Delta\xi})}$ is found to be

509
$$\overline{\left(R_{taa}(\tau_{\Delta\xi}) + R_{taa}{}^*(\tau_{\Delta\xi})\right)\gamma_a(\tau_{\Delta\xi})} = -\frac{2}{c}\frac{\Delta\rho_x\tan\phi}{{M'_{t0}}^3}\exp\left(-\frac{\left(2\Delta\rho_x\tan\phi/c\right)^2}{2{\sigma_{\gamma a2}}^2{M'_{t0}}^2}\right). \quad (48)$$

510 The following term in Eq. (16) is no longer zero and is found to be

511
$$\int d^2\boldsymbol{\rho}\int d^2\Delta\boldsymbol{\rho} b_2(\boldsymbol{\rho},z) b_2(\boldsymbol{\rho}+\Delta\boldsymbol{\rho},z)\overline{\delta\psi}\,\overline{\left(R_{taa}(\tau_{\Delta\xi}) + R_{taa}{}^*(\tau_{\Delta\xi})\right)\gamma_a(\tau_{\Delta\xi})}\left|F_w(\Delta\boldsymbol{\rho})\right|^2$$
$$= (2/c)^2(z\tan\theta_T\tan\phi)^2\Big/\left({M_{sp}}^2{M_t}^3\right). \quad (49)$$

512 To arrive at Eqs. (37) and (39), $\sum_{l=1}^{n_p}\overline{K_s^{(l)}}\,\overline{\delta T_s^{(l)}} = 0$ and $\sum_{l=1}^{n_p}\overline{\Delta t^{(l)}}\,\overline{K_s^{(l)}}\,\overline{\delta T_s^{(l)}} = 0$ are

513 invoked. Also, $\bar{\hat{\alpha}}_t\sum_{l=1}^{n_p}K_s^{(l)}\Delta t^{(l)} = 0$ and $\bar{\hat{T}}_{sav}\sum_{l=1}^{n_p}K_s^{(l)}\Delta t^{(l)} = 0$ are invoked to derive Eq. (37)

514 and Eq. (39), respectively.

515 **Funding.** NASA Earth Science Technology Office Instrument Incubator Program (IIP-2019-0052).

516 **Acknowledgments.** The authors gratefully acknowledge the support from the NASA Goddard Space Flight Center
517 (GSFC) Internal Research and Development program and the NASA Earth Science Technology Office Instrument
518 Incubator Program. The authors are also indebted to Dr. Xiaoli Sun, Dr. David J. Harding and Dr. Erwan Mazarico of
519 NASA GSFC for fruitful discussions on relevant space-borne lidar instruments.

520 **Disclosures.** The authors declare no conflicts of interest.

521 **Data availability.** No data were generated or analyzed in the presented research.

522 **References**

523 1. J. W. Goodman, "Some effects of target-induced scintillation on optical radar performance," Proc. IEEE **53**,
524 1688-1700 (1965).
525 2. J. W. Goodman, Speckle Phenomena in Optics: Theory and Applications, (2nd ed, SPIE Press, 2020).

3. N. E. Yu, J. W. Choi, H. Kang, D.-K. Ko, S.-H. Fu, J.-W. Liou, A. H. Kung, H. J. Choi, B. J. Kim, M. Cha, and L.-H. Peng, "Speckle noise reduction on a laser projection display via a broadband green light source," Opt. Express **22**, 3547–3556 (2014).
4. B. M. Tsai and C. S. Gardner, "Time-resolved speckle effects on the estimation of laser-pulse arrival times," J. Opt. Soc. Am. A **2**, 649-656 (1985).
5. X. Sun, J. B. Abshire, J. D. Beck, P. Mitra, K. Reiff, and G. Yang, "HgCdTe avalanche photodiode detectors for airborne and spaceborne lidar at infrared wavelengths," Opt. Express **25**, 16589-16602 (2017).
6. C. S. Gardner, "Target signatures for laser altimeters: an analysis," Appl. Opt. **21**, 448-453 (1982).
7. C. S. Gardner, "Ranging performance of satellite laser altimeters," IEEE Trans. Geosci Remote Sens., **30**, 1061-1072 (1992).
8. B. M. Tsai and C. S. Gardner, "Remote sensing of sea state using laser altimeters," Appl. Opt. **21**, 3932-3940 (1982).
9. J. W. Goodman, *Statistical Optics* (John Wiley & Sons, 1985).
10. T. Asakura and N. Takai, "Dynamic laser speckles and their application to velocity measurements of the diffuse object," Appl. Phys. **25**, 179–194 (1981).
11. J. R. Chen, K. Numata, and S. T. Wu, "Error analysis for lidar retrievals of atmospheric species from absorption spectra," Opt. Express **27**, 36487-36504 (2019).
12. B. Smith, H. A. Fricker, N. Holschuh, A. S. Gardner, S. Adusumilli, K. M. Brunt, B. Csatho, K. Harbeck, A. Huth, T. Neumann, J. Nilsson, and M. R. Siegfried, "Land ice height-retrieval algorithm for NASA's ICESat-2 photon-counting laser altimeter," Remote Sens. Environ. **233**, 111352 (2019).
13. C. M. Huang and Y. H. Tseng, "Plane fitting methods of LIDAR point cloud," presented at the Asian Conf. Remote Sensing, Colombo, Sri Lanka, 2008.
14. A. Dabas, P. H. Flamant, and P. Salamitou, "Characterization of pulsed coherent Doppler LIDAR with the speckle effect," Appl. Opt. **33**, 6524-6532 (1994).
15. S. Thomas, T. Fusco, A. Tokovinin, M. Nicolle, V. Michau, and G. Rousset, "Comparison of centroid computation algorithms in a Shack-Hartmann sensor," Mon. Not. R. Astron. Soc. **371**(1), 323–336 (2006).
16. Z. Li and X. Li, "Centroid computation for Shack-Hartmann wavefront sensor in extreme situations based on artificial neural networks," Opt. Express **26**, 31675–31692 (2018).